

Effects of pairwise versus many-body forces on high-stress plastic deformation

B. L. Holian,* A. F. Voter, N. J. Wagner,[†] R. J. Ravelo, and S. P. Chen
Theoretical Division, Los Alamos National Laboratory, Los Alamos, New Mexico 87545

W. G. Hoover and C. G. Hoover
Lawrence Livermore National Laboratory, Livermore, California 94550

J. E. Hammerberg
Applied Theoretical Physics Division, Los Alamos National Laboratory, Los Alamos, New Mexico 87545

T. D. Dontje
Thinking Machines Corporation, Cambridge, Massachusetts 02142
 (Received 29 October 1990)

We propose a model embedded-atom (many-body) potential and test it against an effective, density-independent, pairwise-additive potential in a variety of nonequilibrium molecular-dynamics simulations of plastic deformation under high stress. Even though both kinds of interactions have nearly the same equilibrium equation of state, the defect energies (i.e., vacancy formation and surface energies) are quite different. As a result, we observe significant qualitative differences in flow behavior between systems characterized by purely pairwise interactions versus higher-order many-body forces.

INTRODUCTION

Only in the case of noble gases can the interactions between atoms be described realistically by density-independent, pairwise-additive forces. The repulsive and attractive forces arise from spherical electron clouds that stick close to the nuclei. In metals, however, the electrons are not all localized about the nuclei, and, in fact, the valence electrons are often shared among many ions in the manner of a nearly free-electron gas. This means that the energy depends upon the local electron density, resulting in forces between ions that are many body in character, rather than simply pairwise additive.

The interactions between ions in metals can then be represented approximately by a convenient functional form—the so-called embedded-atom potential.¹ In this approximation, the total potential energy Φ of N ions in arbitrary volume V (overall density $\rho = Nm/V$, atomic mass m) can be computed at about twice the expense of simple pair potentials—even under highly nonequilibrium circumstances such as shock-wave fronts, where locally, the ion density is not at all slowly varying:

$$\Phi = \sum_{i=1}^N \left[\frac{1}{2} \sum_{j \neq i} \varphi(r_{ij}) + \mathcal{F}(\rho_i) \right]. \quad (1)$$

Here φ is a density-independent, pairwise-additive contribution depending only on the distance r_{ij} between particles and \mathcal{F} is the embedding energy, a function of the local embedding density ρ_i at atom i , given by a pairwise sum over all neighboring particles, weighted by a spherical localization function w :

$$\rho_i = \sum_{j \neq i} w(r_{ij}). \quad (2)$$

If the embedding function is linear in the local embedding density, then obviously its contribution will be simply pairwise additive, but if \mathcal{F} is *not* linear in ρ_i then higher-order *many-body* contributions result.

One significant consequence of the nonlinearity of the embedding function is that the energy E_{vac} required to form a vacancy in a solid can be made to be much smaller than the bulk cohesive energy E_{coh} per particle (the two are essentially equal for pair-potential materials). Moreover, the shear elastic moduli C_{12} and C_{44} , for perfect crystals, are identical in the (density-independent) pair-potential approximation, but are *not* equal for the embedded-atom model; the difference $C_{12} - C_{44}$, known as the Cauchy pressure, is in fact noticeably positive for most (cubic) metals.¹ Finally, the binding energy of an atom at a free surface in the embedded-atom model (which we will henceforth abbreviate as EAM) can be significantly higher than for a pair potential material; thus the energy of formation of a free surface for the EAM can be significantly lower than for a pair-potential material.

In this paper, we will exploit the differences between pairwise versus many-body forces in nonequilibrium flows, using the method of molecular dynamics (MD), where the atomic trajectories are solved in the classical approximation (Newton's or Hamilton's equations of motion) on the computer.² In particular, we report here on low- and high-velocity impacts of spheres on walls of similar thickness, as well as homogeneous, but anisotropic expansion of the kind expected in planar spallation experiments. In work reported earlier, the same EAM material has been studied under the conditions of hypervelocity impacts³ and nanometer indentation;⁴ here, we will discuss differences in plastic flow, under a variety of cir-

cumstances, between the EAM and an effective, density-independent pair potential, whose equilibrium equation of state—characterized by the normal density $\rho_0 = Nm/V_0$, cohesive energy E_{coh} , and bulk modulus B_0 —is the same as for the EAM, but whose vacancy-formation energy E_{vac} is nearly three times larger than the EAM value.

In the following section, we describe the EAM we have used. In the sections after that, we report the MD results of low- and high-velocity impacts, respectively, and then discuss homogeneous expansion experiments using MD, followed by conclusions.

MODEL EMBEDDED-ATOM POTENTIAL

Our proposed EAM is constructed from simple analytical functions for the pair-potential contribution φ , the localization function w , and the embedding function \mathcal{F} . One motivation for employing analytical functions is that, at this stage of their development, massively parallel computers, which are extremely useful for large-scale MD simulations, can have communication or memory limitations that make large tables of interactions unfeasible. Since the principal bottleneck in MD simulations is the calculation of forces on atoms due to their local environment, computation time is minimized when φ and w are made as short-ranged as possible. To this end, we employ a cubic spline at the point of maximum attractive force in φ , which makes φ go smoothly to zero for separations $r > r_{\text{max}}$; likewise, w is smoothly truncated at r_{max} .

Within the nearest-neighbor approximation, we can rather easily specify the normal density ρ_0 at zero pressure and temperature (or equivalently, the equilibrium nearest-neighbor separation r_0), the cohesive energy E_{coh} , and the bulk modulus B_0 . First, we insist that the minimum well depth $\chi\epsilon$ of the pair potential occur at r_0 , where χ is the fractional pair-potential contribution to the total cohesion. Second, we require that, at normal density, the embedding function exhibit a minimum that contributes the remaining fraction $1-\chi$ to the cohesive energy; thus, in the nearest-neighbor approximation,

$$E_{\text{coh}} = \frac{1}{2}d(d+1)\epsilon, \quad (3)$$

where d is the dimensionality of the system, i.e., 1, 2, or 3, and the factor $d(d+1)$ is the number of nearest neighbors in the d -dimensional close-packed solid. If $\chi=1$, one obtains only the pair-potential part, without any many-body embedding. We choose the value of χ to be approximately equal to the ratio of vacancy energy to cohesive energy, $E_{\text{vac}}/E_{\text{coh}}$, which for metals is typically between 0.2 and 0.4. Finally, the bulk modulus can be adjusted by varying the choice of pair potential (as is possible with a flexible form such as the Morse potential); in this work, we have chosen a short-range Lennard-Jones potential.

Our version of the Lennard-Jones spline (LJ-spl) potential φ is given by the usual LJ 6-12 form for separations $r < r_{\text{spl}}$:

$$\varphi_{\text{LJ}}(r) = 4\chi\epsilon \left[\left(\frac{\sigma}{r} \right)^{12} - \left(\frac{\sigma}{r} \right)^6 \right], \quad (4)$$

where σ is the point at which the LJ 6-12 potential crosses zero and the minimum is at $r_0 = 2^{1/6}\sigma$. Between r_{spl} and r_{max} , φ is a cubic spline in r^2 :

$$\varphi_{\text{spl}}(r) = -a_2(r_{\text{max}}^2 - r^2)^2 + a_3(r_{\text{max}}^2 - r^2)^3, \quad (5)$$

with a_2 and a_3 chosen such that at $r=r_{\text{spl}}$, $\varphi=\varphi_{\text{spl}}$, $\varphi'=\varphi'_{\text{spl}}$, and $\varphi''=\varphi''_{\text{spl}}=0$ (the inflection point of maximum attractive force). For $r > r_{\text{max}}$, both φ and φ' are zero. The resulting expressions for r_{max} , a_2 , and a_3 are

$$r_{\text{max}}^2 = r_{\text{spl}}^2 \left\{ 5 - 5 \left[1 - \frac{1}{25} \left(9 - \frac{24\varphi}{r_{\text{spl}}\varphi'} \right) \right]^{1/2} \right\}, \quad (6a)$$

$$a_2 = \frac{5r_{\text{spl}}^2 - r_{\text{max}}^2}{8r_{\text{spl}}^3(r_{\text{max}}^2 - r_{\text{spl}}^2)} \varphi', \quad (6b)$$

$$a_3 = \frac{3r_{\text{spl}}^2 - r_{\text{max}}^2}{12r_{\text{spl}}^3(r_{\text{max}}^2 - r_{\text{spl}}^2)^2} \varphi'. \quad (6c)$$

For the LJ-spl potential (in units of σ and ϵ), $r_{\text{spl}} = 1.244455$, $r_{\text{max}} = 1.711238$, $a_2 = 0.5424494\chi$, and $a_3 = 0.09350527\chi$. (This LJ-spl potential differs from the Holian-Evans potential⁵ only in that the spline here is in r^2 rather than r . As a result, no square root or division by r is required in the MD force calculation.) In Fig. 1, we show the LJ-spl potential.

For the embedding (many-body part of our EAM, the local weighting function w is given by

$$w(r) = \frac{1}{d(d+1)e} \left(\frac{r_{\text{max}}^2 - r^2}{r_{\text{max}}^2 - r_0^2} \right)^2, \quad (7)$$

where e is the base of the natural logarithms. The weighting of neighbors looks qualitatively like a Gaussian; beyond r_{max} it is zero (see Fig. 2). At the normal bulk density ($r=r_0$) the local embedding density, as given by the nearest-neighbor approximation, is $\rho_i = 1/e$.

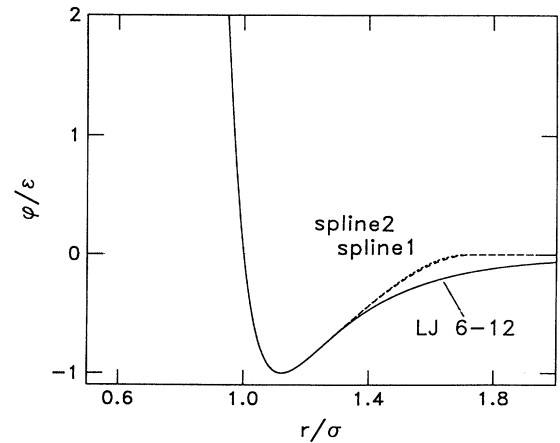


FIG. 1. LJ-spline ($\chi=1$) pair potential φ vs separation r ; σ is the crossing point, the minimum occurs at $r_0 = 2^{1/6}\sigma \sim 1.12\sigma$, and the well depth is ϵ . The cubic spline in r^2 begins at $\sim 1.24\sigma$ and ends at $\sim 1.71\sigma$. (On this scale, a cubic spline in r , labeled “spline 1,” is hardly distinguishable from the spline in r^2 , labeled “spline 2,” lying just slightly above.)

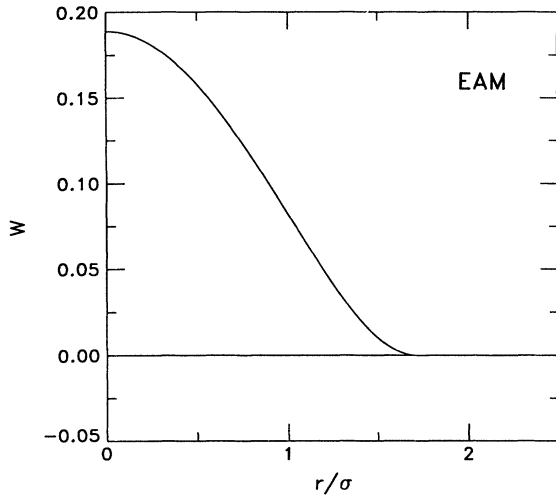


FIG. 2. Local weighting function w for our 2D EAM potential vs separation r . The local embedding density ρ_i for atom i is given by the sum of w over all neighbors of i .

Finally, we have chosen the embedding energy function \mathcal{F} to be a nonlinear function of the form

$$\mathcal{F}(\rho_i) = \frac{1}{2}d(d+1)\epsilon(1-\chi)e\rho_i \ln \rho_i \quad (8)$$

(see Fig. 3). Clearly, at normal density, where the local embedding density is $\rho_i = 1/e$, \mathcal{F} contributes a fraction $1-\chi$ to the total cohesive energy (in the nearest-neighbor approximation).

If the LJ-spl pair-potential fractional contribution to the cohesive energy is $\chi = \frac{1}{3}$, then in three dimensions (3D) this EAM many-body potential, given by Eqs. (4)–(8), is a reasonably good potential for copper or nickel (see Table I). In fact, the equation of state for our

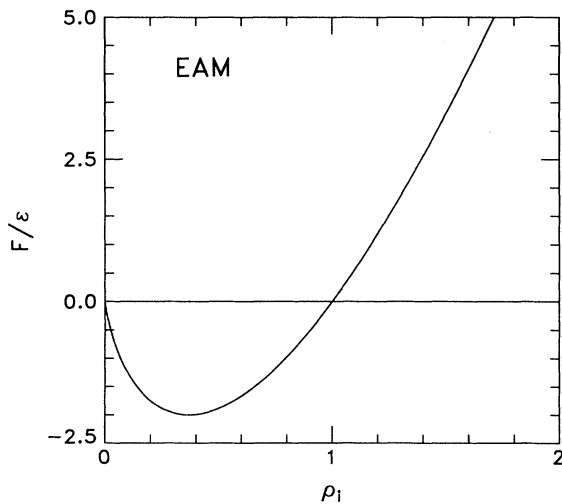


FIG. 3. Embedding energy function \mathcal{F} for our ($\chi = \frac{1}{3}$) 2D EAM potential vs local density ρ_i . The minimum occurs at $\rho_i = e^{-1}$.

TABLE I. Comparison of properties of our 3D EAM with Cu and Ni;⁹ $\alpha = (9B_0V_0/2NE_{\text{coh}})^{1/2}$ [see Eq. (10)]. The nearest-neighbor approximation to EAM is indicated by NN.

	α	$\frac{E_{\text{vac}}}{E_{\text{coh}}}$	$\frac{C_{12} - C_{44}}{B_0}$
EAM	4.11	0.33	0.27
EAM (NN)	3.84	0.36	0.19
Cu	3.65	0.37	0.30
Ni	3.53	0.36	0.12

EAM material, over a range of densities near ρ_0 and for temperatures not too high, can be approximated by that of an effective, density-independent pair potential, for which ρ_0 , E_{coh} , and B_0 are chosen to reproduce the EAM values. For example, we can construct a short-range (spline) pair potential in exactly the same manner as shown above in Eq. (6) for the LJ-spl potential, substituting instead the more flexible Morse form

$$\varphi_{\text{Morse}}(r) = \epsilon \{ \exp[-\alpha(r/r_0 - 1)] - 1 \}^2 - \epsilon, \quad (9)$$

where the steepness of the repulsive wall is given in the nearest-neighbor approximation by

$$\alpha = \left[\frac{d^2 B_0 V_0}{2NE_{\text{coh}}} \right]^{1/2}. \quad (10)$$

(The LJ-spl potential can be reasonably well approximated by the spline Morse potential, with $\alpha = 6$.) In 2D, we find that $\alpha \approx 4.5$ gives a good fit to the cold curve (Φ versus ρ at $T=0$) for our EAM system, as shown in Fig. 4. We also find that the EAM shock Hugoniot can be

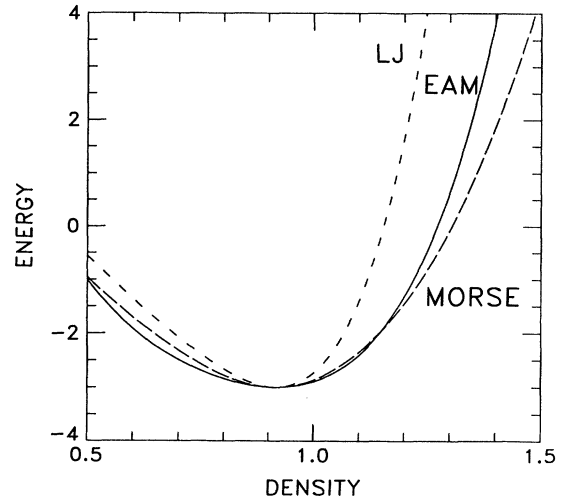


FIG. 4. Two-dimensional cold curve ($T=0$ K) of internal energy (per atom, in units of ϵ) as a function of density $\rho = Nm/V$ (units of m/σ^2 , m is the atomic mass) for the LJ-spl ($\chi=1$), EAM ($\chi=\frac{1}{3}$), and Morse ($\alpha=4.5$) potentials. The normal density (at $P=T=0$) for all three potentials is $\rho_0 = \sqrt{4/3}m/r_0^2 = 0.916m/\sigma^2$. The cohesive energy for all three materials is 3ϵ . The nearest-neighbor approximation to the bulk modulus for the EAM potential is given by $B_0V_0/N\epsilon = 22.1$, compared to 54 for the LJ-spl.

predicted from the Morse potential parameters, at least for shocks that are not too strong.⁶ On the other hand, the Morse vacancy formation energy is $E_{\text{vac}} \approx 3\epsilon$, while the EAM value is much lower, namely, about 1.2ϵ . The ease of vacancy formation may well be an important factor in the noticeably lower melting temperature of the 2D EAM solid, which is $kT_m/\epsilon=0.2$, compared with 0.35 for the Morse potential and 0.4 for the LJ-spl potential. As we will show in the following sections, these defect energy differences—for free surfaces, dislocations, and vacancies—dramatically affect the flow characteristics of the many-body versus pairwise systems.

LOW-VELOCITY IMPACTS

First, we studied the impact of a 2D sphere (i.e., disk) hitting a wall (both ball and wall are made of the same kind of atoms) at a velocity low enough to cause significant deformation, but not high enough to penetrate the wall. The ratio of sphere diameter to wall thickness was about 2.4, and the relative velocity at impact was $u_p = \sqrt{\epsilon/m}$, about one-fifth the longitudinal speed of sound (c_0 is $\sim 5\sqrt{\epsilon/m}$ for both the EAM and Morse potential, as compared to $\sim 9\sqrt{\epsilon/m}$ for the LJ-spl potential).

The ball does not rebound elastically, but rather, cold welds to the wall. In Fig. 5, we show the final state of a sphere of 1200 pair-potential atoms. (Both ball and wall were initially perfect lattices at a temperature $kT/\epsilon=0.05$.) Considerable plastic flow has occurred; note the distortion in the shape of the ball and the roughness of the back of the wall. Several dislocations have been created in the wake of the shock waves and subsequent rarefactions following impact. However, the EAM system in Fig. 6 shows some dramatic differences in its

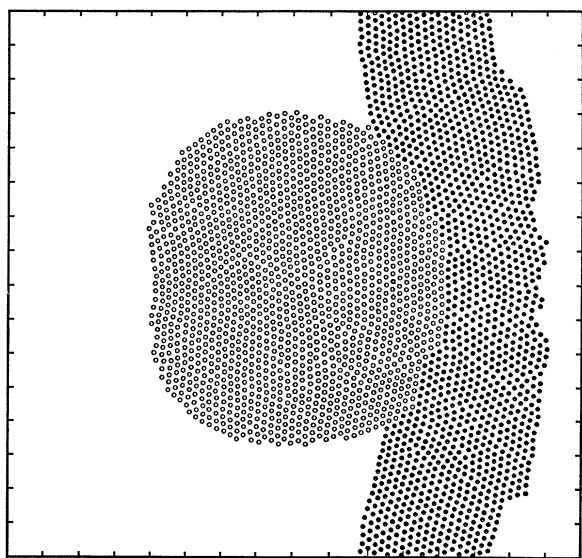


FIG. 5. Low-velocity impact of a 2D 1200-atom ball (open circles) onto a wall 40% as thick (solid circles) for the Morse ($\alpha=4.5$) pair potential, at a velocity one-fifth that of sound, after a time of $25t_0$ (t_0 is the fundamental unit of time, given by $\sigma\sqrt{m/\epsilon}$).

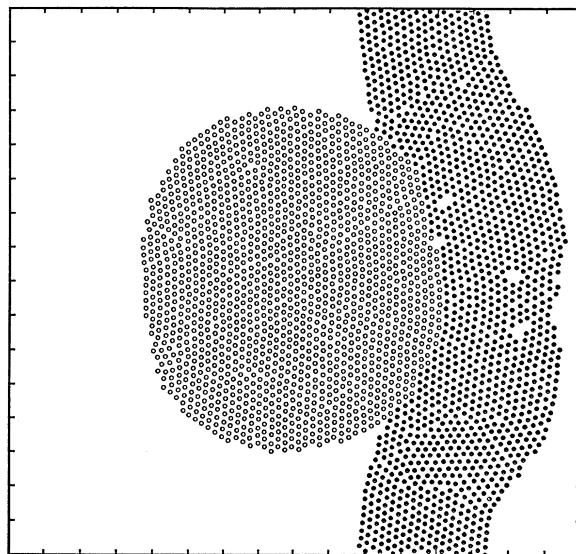


FIG. 6. The same as Fig. 5, but for the EAM many-body potential. Note the enhanced number of vacancies compared with the pair-potential material in Fig. 5.

response to the impact: (i) the ball shows less distortion and the wall has a smoother back surface; (ii) incipient cracks have formed in the wall near the edges of the impact crater; and (iii) in addition to several dislocations, four distinct (di)vacancies have been created in the EAM case, in marked contrast to their absence in the pair-potential system. (We have noted the propensity of the EAM system to generate vacancies in a variety of non-equilibrium situations, far in excess of the equilibrium population. Presumably, most of these vacancies anneal out on long diffusional time scales.) A computer-generated movie enhances one's impression that significantly more plastic flow occurs in a material characterized by many-body interactions, compared with a purely pair-potential material.

HYPERVELOCITY IMPACTS

In earlier work, we reported on MD calculations of hypervelocity impacts,³ in which the velocity of an impacting ball is large enough to penetrate a thinner wall (thickness 40% of the diameter of the ball) and create an expanding bubble of debris behind the plate. We considered a ball of 700 LJ-spl atoms hitting a wall of 8000 (LJ-spl) atoms in 3D, and observed that, in contrast to laboratory (macroscopic) experiments, such small MD systems in 3D result in debris clouds that are densest at their centers, rather than being hollow. We then tested our speculation that an order of magnitude more particles would be needed to see the appropriate continuum behavior by performing 2D calculations of 500, 1500, and 5000 ball atoms (N atoms in 2D correspond to $N^{3/2}$ atoms in 3D at the same density—thus 5000 atoms in 2D scale to one-third of a million atoms in 3D). The results confirmed our speculation, perhaps even more dramati-

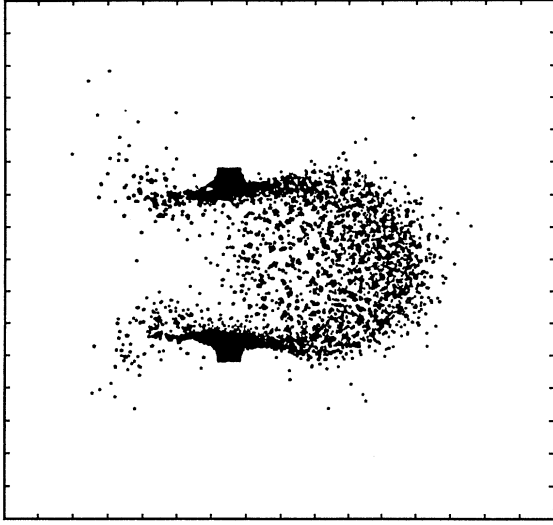


FIG. 7. Hypervelocity impact and penetration of 2D 5000-atom ball onto a wall 40% as thick for the Morse ($\alpha=4.5$) pair potential, at a velocity twice that of sound, after a time of $30t_0$.

cally than we had anticipated. Namely, we found that on the order of 1000 ball atoms were necessary to exhibit continuumlike behavior in 2D, corresponding to roughly 30 000 atoms in 3D. (This kind of convergence to the continuum limit was also subsequently seen in the indenter MD calculations.⁴) In this paper, we report on an additional comparison between our EAM (many-body) material and the Morse pair-potential system for the same hypervelocity impacts.

In Fig. 7, we see the debris cloud generated by a hypervelocity impact at velocity $u_p = 12\sqrt{\epsilon/m}$ of 5000 ball

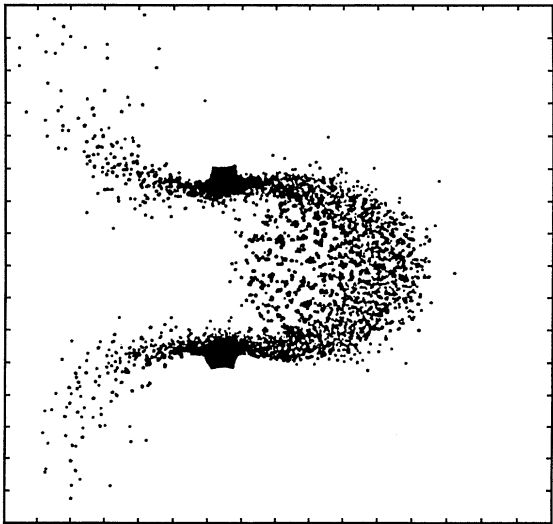


FIG. 8. The same as Fig. 7, but for the EAM many-body potential. Note the difference in shape and clustering compared to the pair-potential material in Fig. 7. Both debris bubbles are hollow and correspond to about 30 000 atoms in 3D.

atoms on 9000 wall atoms, after a time of $30t_0$ (t_0 is the fundamental unit of time, given by $\sigma\sqrt{m/\epsilon}$). The material is characterized by the Morse pair potential. Note that the cloud is hollow, but quite spherical in shape. By contrast, in Fig. 8 for the many-body EAM material, the nose of the debris cloud is more pointed in the direction of the impact, the backsplash is more pronounced, and the skin of the debris bubble is more well-defined. Also, the EAM material clusters more easily than its Morse counterpart. At intermediate velocities between the low-velocity impact of the previous section and the high-velocity impact shown here, the EAM material shows signs of ductile hole growth before fragmenting.⁶

HOMOGENEOUS EXPANSION

In previous work on fragmentation of fluids,⁷ we introduced a method for simulating the adiabatic (constant energy), homogeneous, isotropic expansion of a fluid by molecular dynamics. Here, we specialize that approach to the case of *anisotropic* expansion, which would be appropriate for the case of planar spall following the shock impact of a thin flier plate upon a thicker target plate. After the shock waves emanating from the impact surface hit the opposite free surfaces, rarefaction (tension) waves propagate back toward the center and meet at the spall plane. The tension waves add up, and if they are of sufficient magnitude (i.e., the stress exceeds the spall strength of the material), then the target plate breaks off a piece approximately the size of the incident flier plate. The original shock wave is very sharp, while the rarefaction waves spread out and decay in magnitude as they travel. Nevertheless, both the drop in strain rate $\dot{\epsilon}_{xx}$ when the shock passes and the rise when the rarefaction fan goes by are relatively rapid compared to the slow decay in strain rate afterwards. Therefore, it is reasonable to approximate the process of spallation that follows some longer time later as adiabatic (constant energy). Thus, the kinetic energy of expansion in a large region around the spall plane is the dominant feature to be considered. We can simulate this feature by considering a periodically repeated volume whose length in the x direction grows at a constant rate, namely, $\dot{L}_x(t) = 2u_p$ (by convention, the boundary velocity u_p is taken to be positive in compression). Also, at $t=0$, a homogeneous velocity gradient is superimposed on the equilibrium thermal velocities of particles, in the form $\dot{x} = \dot{\epsilon}_{xx}x$, where $\dot{\epsilon}_{xx}(0) = -2u_p/L_x(0)$ is the initial strain rate. Afterwards, Newton's equations of motion are followed, with crossings of the periodic volume in the x direction (at $+L_x/2$ and $-L_x/2$) accompanied by changes of $+2u_p$ and $-2u_p$, respectively. Except for the occasional imbalances of particle crossings at the periodic boundaries, the total energy is constant in time. The strain rate as a function of time is then

$$\dot{\epsilon}_{xx}(t) = \frac{\dot{L}_x(t)}{L_x(t)} = -\frac{2u_p}{L_x(t)} = \frac{\dot{\epsilon}_{xx}(0)}{1 + \dot{\epsilon}_{xx}(0)t}. \quad (11)$$

In order to achieve an annealed granular crystal in 2D, we used two schemes. In the first, we melted a perfect

triangular lattice (where particles were located initially at lattice sites with random velocities chosen from a Maxwellian distribution whose temperature was ten times the melting temperature), and equilibrated the resulting fluid using the time-reversible Nosé-Hoover (NH) thermostat.⁸ Then, we quenched the system to a temperature well below the freezing point, again using the NH thermostat, with a thermostat response time that was comparable to the Einstein vibrational period $\sim 0.75t_0$. After several vibrational periods, the fine-grained, almost amorphous material obtained from the melt annealed into the granular sample shown in Fig. 9(a) (2D LJ-spl). Notice the well-defined grain boundaries, which have been pretty well stabilized. In the second method of annealing, we have placed the atoms on *unstable* lattice sites, namely, on a square lattice at the appropriate density. Now, rather than melting, the system almost instantaneously transforms itself into a very fine-grained triangular polycrystal, which then anneals in a similar fashion to the initially fluid system. In either case, the sample is then subjected to the plane-strain boundary and initial conditions described above for modeling spallation. While the initial conditions, including specific grain boundaries, dislocations, vacancies, and interstitials, are dependent in detail on the thermal fluctuations, the *qualitative* nature of the subsequent fracture we observe is not affected strongly by them, as various sample calculations have shown.

In Fig. 9(b), we show the resulting cracks in a polycrystalline 2D LJ-spl system that have opened up after several vibrational periods, for a strain rate of $\dot{\epsilon}_{xx}(0)t_0 = 0.025$. Thus the strain rate chosen here, while comparable to those in strong shock waves, is nevertheless small enough that the expansion velocity of a pair of neighboring atoms is a tiny fraction of the sound speed c_0 . As can be seen from Fig 9(b), the cracks begin almost simultaneously to open up, primarily along (vertical) grain boundaries. A computer-generated movie of this process shows that, even though the grain size in these calculations is extremely small, dislocations are emitted from some of the crack tips, helping to heal them up. Clearly, with only 4000 atoms, it is not possible to say anything definitive about the possibility of *intragranular* fracture. We have done calculations on larger systems that are made possible by massively parallel computers and we defer discussion of this topic to a planned forthcoming paper.⁶

We can, however, say that there are some notable differences when these homogeneous expansion calculations are done for EAM materials, as shown in Fig. 9(c). Recalling the smoother surfaces observed in the low-velocity impact, the EAM cracks are much smoother (more spherical), as might be expected in a more ductile material. The EAM material is much more plastic than its pair-potential counterpart, resulting in a 50% larger strain before fracture. This difference in plasticity is exaggerated in 2D compared to 3D. The formation energy of a dislocation in 2D is like that of a single vacancy, while in 3D, it is more like a line of vacancies. More work needs to be done for larger systems before we can give a reliable estimate of the spall strengths of the two materials.⁶

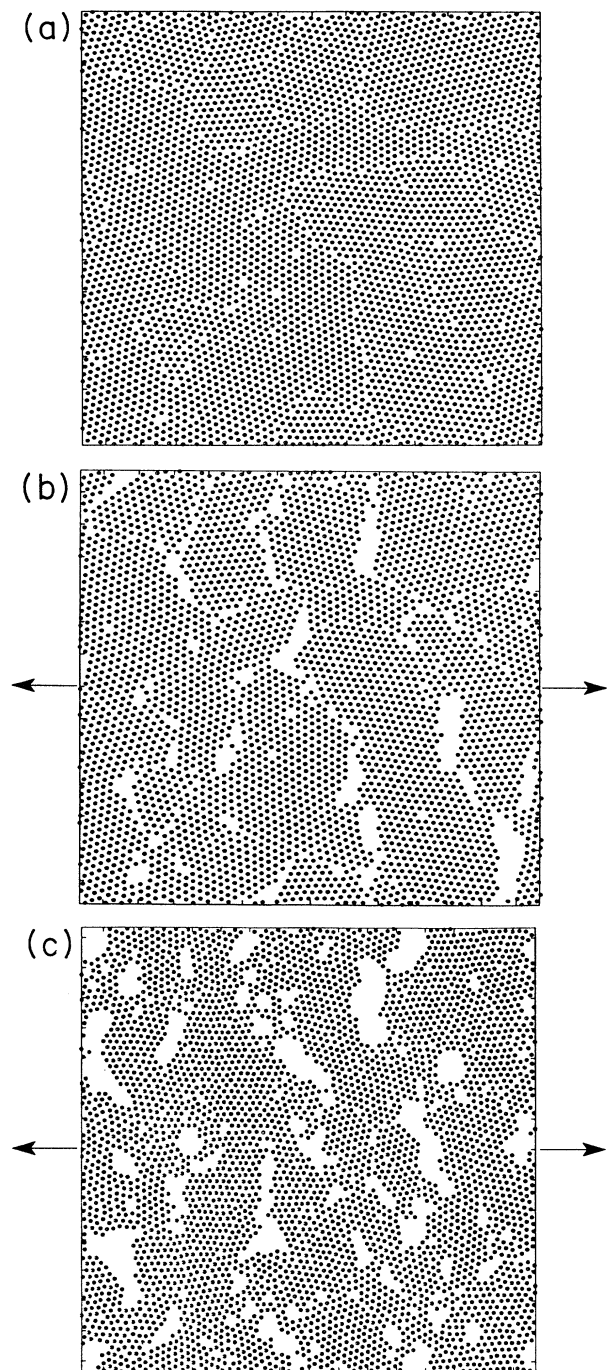


FIG. 9. Fracture in multigranular 2D crystals: (a) 4000 atoms, interacting by the short-range LJ-spl potential, after melting and quenching to about $\frac{1}{4}$ the melting temperature; the annealing process has taken about 20 mean vibrational periods. (b) A snapshot of the LJ-spl system taken after about six periods following the onset of a homogeneous expansion (plane strain) in the horizontal direction (the rate of expansion times the fundamental period is about 2%); fracture has begun primarily in the vertical direction along grain boundaries. (c) A snapshot of the EAM system under similar initial conditions and the same boundary conditions as in (b); note the more spherical shapes of the cracks.

CONCLUSIONS

We have shown that the influence of many-body forces, as opposed to simple pairwise-additive forces, can enhance plastic flow. We have studied this effect by comparing a pairwise to a many-body interaction, both of which give very similar equations of state—at least near normal density. At low-velocity impacts, the EAM (many-body) potential gives the expected enhancement in the number of vacancies formed, as well as the appearance of smoother surfaces, than the Morse (pairwise) potential. At high velocities, the skin depth of the debris bubble (produced by penetration of the projectile) is more pronounced for the EAM than the Morse material. The damage under tensile loading can be simplified by assuming homogeneous adiabatic expansion; then, the two materials also show differences in the cracks that form. In the case of the Morse potential, the cracks are sharp and brittle looking, while the EAM cracks look more like ductile holes. In future studies, we will examine the size

dependence of these qualitative observations of plastic response, in 3D as well as 2D.

ACKNOWLEDGMENTS

This work was supported by both ISRD (Institutionally Supported Research and Development) funds and by the armor/antiarmor program at Los Alamos; as such, we owe a significant debt of gratitude to Ed Cort for his continuous encouragement and helpful suggestions. At Livermore, Irv Stowers deserves particular mention for his support of the Hoover work on the indenter problem. We also gratefully acknowledge helpful discussions with Tony Rollett, Fred Kocks, Paul Follansbee, Phil Howe, Paul Taylor, Brian Dodson, David Srolovitz, and Dennis Grady. This work was performed under the auspices of the University of California for the U.S. Department of Energy at Los Alamos, under Contract No. W-7405-Eng-36, and at Livermore, under Contract No. W-7405-Eng-48.

*Author to whom correspondence should be addressed at T-12, MS-B268, Los Alamos National Laboratory, Los Alamos, NM 87545.

†Present address: Department of Chemical Engineering, University of Delaware, Newark, DE 19716.

¹M. S. Daw and M. I. Baskes, *Phys. Rev. B* **29**, 6443 (1984); S. M. Foiles, M. I. Baskes, and M. S. Daw, *ibid.* **33**, 7983 (1986); see also, R. A. Johnson, *ibid.* **37**, 3924 (1988).

²See, for example, W. G. Hoover, *Molecular Dynamics* (Springer-Verlag, Berlin, 1986); see also selections from *Molecular Dynamics Simulation of Statistical-Mechanical Systems*, Proceedings of the International School of Physics "Enrico Fermi," Summer School Course 97, edited by G. Ciccotti and W. G. Hoover (North-Holland, Amsterdam, 1986).

³B. L. Holian, in *Microscopic Simulation of Complex Flows*, Vol.

236 of *NATO Advanced Study Institute, Series B: Physics*, edited by M. Mareschal (Plenum, London, 1991); *Phys. Rev. A* **36**, 3943 (1987); for a discussion of continuum calculations of hypervelocity impacts, see also K. S. Holian and B. L. Holian, *Int. J. Impact Eng.* **8**, 115 (1989).

⁴W. G. Hoover, A. J. De Groot, C. G. Hoover, I. F. Stowers, T. Kawai, B. L. Holian, T. Boku, S. Ihara, and J. Belak, *Phys. Rev. A* **42**, 5844 (1990).

⁵B. L. Holian and D. J. Evans, *J. Chem. Phys.* **78**, 5147 (1983).

⁶B. L. Holian, A. F. Voter, N. J. Wagner, R. J. Ravelo, S. P. Chen, J. E. Hammerberg, and T. D. Dontje (unpublished).

⁷B. L. Holian and D. E. Grady, *Phys. Rev. Lett.* **60**, 1355 (1988).

⁸B. L. Holian, A. J. De Groot, W. G. Hoover, and C. G. Hoover, *Phys. Rev. A* **41**, 4552 (1990).

⁹See experimental references in S. M. Foiles, M. I. Baskes, and M. S. Daw, *Phys. Rev. B* **33**, 7983 (1986).